Satellite Aerosol Retrieval From Multiangle Polarimetric Measurements: Information Content and Uncertainty Analysis

Wenhui Dong, Minghui Tao, Xiaoguang Xu, Jun Wang, Yi Wang, Lunche Wang, Yinyu Song, Meng Fan, and Liangfu Chen

***Abstract*— The multiangle polarimetric (MAP) instruments have been a focus of recent satellite missions dedicated to enhanced detection of global aerosol microphysical properties. Considering that satellite observations can hardly infer all the unknowns of atmosphere and surface, it is crucial to know how many and which aerosol parameters can be accurately retrieved from these different MAP measurements as well as their uncertainties. In this study, we present a comprehensive insight into the information content of POLarization and Directionality of Earth Reflectance-3 (POLDER-3) and multiviewing, multichannel, multipolarization imager (3MI) observations for aerosol retrievals and estimate posterior errors of corresponding parameters based on the Bayesian theory. The total degree of freedom for signal (DFS) of aerosol retrievals is around 6–8 from POLDER-3 and is raised by ∼1.8–3.5 with 3MI. The retrieval accuracy of volume concentration and effective radius is high (<4%) in the fine-dominant case for both POLDER-3 and 3MI but gets much lower (∼8% and ∼15%) in coarse-dominant conditions. Furthermore, the advanced 3MI measurements can upgrade the retrieval uncertainties of POLDER-3 by ∼50%. Though additional shortwave infrared bands of 3MI provide more information regarding coarse particles, the influence of aerosols on surface bidirectional reflectance distribution function (BRDF) leads to a decrease in the total DFS. With a prior assumption that variations of refractive index depend on wavelength, satellite retrieval accuracy of the real part (MR) (<0.03) and imaginary part (MI) (<0.003) reaches close levels with that of ground-based Sun photometers. Our results can provide a fundamental reference for MAP satellite retrieval of aerosol microphysical properties.**

***Index Terms*— Information contents, multiangle polarimetric (MAP) measurements, posterior errors, retrieval of aerosol microphysical parameters.**

I. Introduction

ATMOSPHERIC aerosols are mixtures of small particles with different sizes and components. By changing solar radiation and modifying cloud properties [1], these tiny particles play a critical role in regulating energy balance and hydrologic cycle of the Earth's atmosphere system [2], [3]. Moreover, fine particles near surface at a high concentration have adverse effects on public health, which have been proven to have a robust correlation with morbidity and mortality of respiratory and cardiovascular diseases [4]. Due to short lifetimes (∼hours to days) and complex emission sources, the amount as well as physical and chemical properties of aerosols vary largely over space and time [5], [6]. By now, the climate and environmental effects of aerosols suffer from considerable uncertainties due to largely the lack of accurate information regarding different aerosol types at regional and global scales [7].

Since the late 1990s, several dedicated satellite instruments, such as Moderate Resolution Imaging Spectroradiometer (MODIS), Multiangle Imaging SpectroRadiometer (MISR), and POLarization and Directionality of Earth Reflectance (POLDER), have been launched to monitor global aerosols over land [8]. The satellite aerosol products have greatly renewed knowledge of global aerosol emission sources and hotspots. However, each satellite-measured signal at the top of atmosphere (TOA) is from two complicated objects of aerosol and surface, the angular and spectral backscattering of which both need more than one unknown parameter to constrain. Thus, priori assumption or simplification is usually adopted in aerosol/surface scattering modeling and satellite aerosol retrieval. Because of limited information, multispectral satellite observation mainly retrieves aerosol optical depth (AOD) with fixed aerosol models in lookup tables and precalculated surface reflectance or their linear relationships. By contrast, satellite measurements with additional multiangle polarimetric (MAP) information can also retrieve aerosol size and refractive index by optimized fitting with iterative calculation of radiative transfer model [9]. Despite the obvious sensitivity to aerosol optical/microphysical properties, it is crucial to determine

Manuscript received 16 October 2022; revised 26 December 2022 and 15 February 2023; accepted 17 March 2023. Date of publication 5 April 2023; date of current version 19 April 2023. This work was supported by the National Natural Science Foundation of China under Grant 41830109 and Grant 42271382. *(Corresponding author: Minghui Tao.)*

Wenhui Dong, Minghui Tao, Yi Wang, Lunche Wang, and Yinyu Song are with the Key Laboratory of Regional Ecology and Environmental Change, School of Geography and Information Engineering, China University of Geosciences, Wuhan 430074, China (e-mail: dong_wenhui@cug.edu.cn; taomh@cug.edu.cn; wangyi34@cug.edu.cn; wang@cug.edu.cn; evelynsong@cug.deu.cn).

Xiaoguang Xu is with the Department of Physics, GESTAR-II, and Earth and Space Institute, University of Maryland, Baltimore County, Baltimore, MD 21250 USA (e-mail: xxu@umbc.edu).

Jun Wang is with the Center for Global and Regional Environmental Research, The University of Iowa, Iowa City, IA 52242 USA (e-mail: jun-wang-1@uiowa.edu).

Meng Fan and Liangfu Chen are with the State Key Laboratory of Remote Sensing Science, Aerospace Information Research Institute, Chinese Academy of Sciences, Beijing 100101, China (e-mail: fanmeng@aircas.ac.cn; chenlf@aircas.ac.cn).

This article has supplementary downloadable material available at https://doi.org/10.1109/TGRS.2023.3264554, provided by the authors.

Digital Object Identifier 10.1109/TGRS.2023.3264554

which parameters can be accurately inversed from specific MAP measurements before establishing retrieval strategy and priori constraints.

The global measurements of POLDER-3 aboard PARASOL (Polarization and Anisotropy of Reflectances for Atmospheric Sciences coupled with Observations from a Lidar) satellite during 2004–2013 have promoted the development of MAP retrievals of aerosol optical/microphysical parameters. With the successful inversion and application of POLDER-3 aerosol products, new MAP instruments, such as directional polarimetric camera (DPC) series on Chinese GaoFen-5 satellite, have been increasing quickly [10]. As an enhanced version of POLDER-3, the multiviewing, multichannel, multipolarization imager (3MI) mission will have improved spatial coverage (2200 km), higher spatial resolution (4 km at nadir), and an expanded spectral range (410–2130 nm) with 9 of the 12 spectral bands having polarized measurements [11]. Although optimized inversion of the same aerosol parameters can be conducted using these MAP measurements, their distinct aerosol information content can exert a challenge on consistency of corresponding accuracy and availability.

While MAP instruments, such as POLDER-3, have shown great potential in obtaining aerosol microphysical parameters [12], [13], the information content of MAP measurement can be very different depending on instrument settings and observation modes. For instance, a single-view and five-band cloud and aerosol polarimetric imager (CAPI) onboard Chinese Carbon Dioxide (CO_2) Observation Satellite can only provide 3–4.5 pieces of aerosol information, including total volume, fine mode fraction, and imaginary part (MI) of refractive index for coarse particles [14]. Also, MAP measurements have distinct sensitivities to different aerosol optical/microphysical properties. The optimized retrieval using MAP satellite observations usually includes more than 20 aerosol and surface parameters, and the insensitive ones selected can transmit the corresponding uncertainties to the overall inversion [15]. On the other hand, different retrieved parameters and assumptions are usually adopted in optimized inversion [16], [17], leading to difficulty in their comparison and consistency. To ensure a reliable and consistent MAP inversion of interested aerosol parameters, it is necessary to make a comprehensive estimation of their information content and assign a pertinent degree of freedom or constraints.

To explore the optimal detection ability of specific satellite instruments, it is essential to estimate their information content or sensitivity with respect to retrieved aerosol and surface parameters [18]. As the primary error source in retrieval of greenhouse gases such as CO_2, many efforts have been made to analyze aerosol information content in the hyperspectral remote sensing of Orbiting Carbon Observatory-2 (OCO-2)/ Greenhouse Gases Observing Satellite (GOSAT) [19], [20] or from accompanied aerosol detection instrument such as CAPI. Moreover, retrieval feasibility and potential, such as aerosol layer height from MAP measurements in oxygen O_2 A and O_2 B bands, can be tested by the estimation of information content and posteriori errors [21]. However, previous studies mostly focus on satellite instruments not dedicated for aerosols. By now, to what extent and which aerosol optical/microphysical parameters can be accurately retrieved from common MAP measurements such as POLDER-3 and enhanced 3MI have been rarely fully concerned.

In this study, we present a comprehensive insight into the information content of typical satellite MAP measurements, and the degree of freedom and posteriori error of common aerosol microphysical parameters based on radiative transfer simulation and Bayes optimization theory. The information content of POLDER-3 and 3MI observations is estimated and compared. Section II introduces the theory of information and inversion. The configuration of forward simulations, assumptions, and priori knowledge is described in Section III. Then, information content and retrieval errors of the aerosol parameters are analyzed and discussed in Section IV. Finally, we summarize the main results and conclusions.

II. Theory of Information and Inversion

The basic premise of inversion is to establish a forward model ($\mathbf{F}$) that can describe the physical process from the Sun and the Earth's atmosphere to satellite measurements. Let $\mathbf{x}$ represent a state vector that includes n variables to be retrieved (e.g., aerosol microphysical and surface reflective parameters) and $\mathbf{y}$ represent the observation vector that contains m measurement elements. Then, satellite measurements can be expressed as

$$\mathbf{y} = \mathbf{F}(\mathbf{x}) + \epsilon \tag{1}$$

where ϵ denotes experimental errors from both satellite measurements and forward model. If ϵ fit the Gaussian probability distribution function (PDF) and the forward model (e.g., usually the radiative transfer model) is linear in the proximity of the true state, a maximum likelihood solution (also called retrieval or posteriori) of the state vector according to the Bayesian optimal estimation theory [22] is

$$\hat{\mathbf{x}} = \mathbf{x}_a + \left(\mathbf{K}^{\mathrm{T}}\mathbf{S}_{\epsilon}^{-1}\mathbf{K} + \mathbf{S}_a^{-1}\right)^{-1}\mathbf{K}^{\mathrm{T}}\mathbf{S}_{\epsilon}^{-1}(\mathbf{y} - \mathbf{K}\mathbf{x}_a) \tag{2}$$

where $\mathbf{S}_a$ is the error covariance matrix of the prior state vector $\mathbf{x}_a$ that provides knowledge of the state before measurement. $\mathbf{S}_{\epsilon}$ is the measurement error covariance matrix. $\mathbf{K}$ is the $m \times n$ Jacobian matrix consisting of partial derivatives of each measurement with respect to each state element ($\partial F/\partial x$). The retrieval of state vector, $\hat{x}$, is usually not unique and has a fluctuation following Gaussian PDF. The posterior error covariance matrix $\hat{\mathbf{S}}$ describes the statistical uncertainties of $\hat{\mathbf{x}}$ due to errors from observation, forward modeling assumptions, and a prior. The square roots of the diagonals of $\hat{\mathbf{S}}$ represent the 1σ uncertainties of the retrieved parameters

$$\hat{S}^{-1} = \mathbf{K}^{\mathrm{T}}\mathbf{S}_{\epsilon}^{-1}\mathbf{K} + \mathbf{S}_a^{-1}. \tag{3}$$

The averaging kernel matrix is defined by derivatives of the posterior state vector with respect to the true state ($\mathbf{A} = (\partial\hat{x}/\partial\mathbf{x})$), which has been widely used to quantify the information obtained via measurement and the sensitivity of the inversion to the true state. An identity $\mathbf{A}$ matrix means a perfect retrieval, while a null $\mathbf{A}$ indicates that the

$$\mathbf{A} = \frac{\partial\hat{x}}{\partial\mathbf{x}} = \left(\mathbf{K}^{\mathrm{T}}\mathbf{S}_{\epsilon}^{-1}\mathbf{K} + \mathbf{S}_a^{-1}\right)^{-1}\mathbf{K}^{\mathrm{T}}\mathbf{S}_{\epsilon}^{-1}\mathbf{K} \tag{4}$$

measurements obtain no information of the inversion parameters. The trace of the **A** matrix is defined as the degree of freedom for signal (DFS), denoting independent pieces of information gained from all the measurements. Correspondingly, the diagonal elements of **A** represent the sensitivity of each retrieved parameter to its truth.

Furthermore, the error-normalized (EN) Jacobian matrix is used to estimate the effective sensitivity of a single measurement to each retrieval parameter

$$\tilde{K} = \mathbf{S}_\epsilon^{-\frac{1}{2}} \mathbf{K} \mathbf{S}_a^{\frac{1}{2}}. \tag{5}$$

EN Jacobian matrix compares the observation error with the variability of the observation vector that is expressed by its prior covariance ($\mathbf{KS}_a^{(1/2)}$). If the natural variability of observation vector is less than its error (e.g., $\tilde{\mathbf{K}}_{i,j} < 1$), the measurement y_i does not have useful information for retrieving parameter x_j. By contrast, the greater the value when $K_{i,j} > 1$, the more useful information the measurement y_i has in the retrieval of x_j. To make the information content analysis and inversion linear and easy to calculate, both $\mathbf{S}_\epsilon$ and $\mathbf{S}_a$ are usually assumed to be independent between measurements and retrieved parameters, respectively, to get a zero off-diagonal matrix.

III. Simulation of Satellite Measurements

A. MAP Satellite Measurements and Observation Vector

POLDER-3 takes MAP measurements at nine bands (443, 490, 565, 670, 763, 765, 865, 910, and 1020 nm) with three of which are polarized (490, 670, and 865 nm), a swath width of ~1600 km, and a spatial resolution of 5.3 × 6.2 km at nadir [23]. POLDER-3 can observe the surface target by up to 16 (14 on average) viewing directions (cross track ±43° and along track ±51°). As an improved version of POLDER-3, 3MI extends the spectral range by adding deep blue (410 nm) and shortwave infrared bands (1650 and 2130 nm) to enhance aerosol detection such as coarse particles. The 1020 nm band of POLDER-3 is replaced by 1370 nm to improve the detection of cirrus cloud. Moreover, 3MI measurements are polarized in most bands except 754, 763, and 910 nm. Besides 14 viewing angles similar to POLDER-3, 3MI has a larger swath width of ~2200 km and a higher spatial resolution of 4 km.

Compared with polarize radiance or reflectance, degree of linear polarization (DOLP) has higher accuracy as a relative quantity

$$\mathrm{DOLP} = \frac{\sqrt{Q^2 + U^2}}{I}. \tag{6}$$

The 910 nm water vapor absorption band is not used in aerosol remote sensing. Since the two O_2 A bands around 765 nm have limited information regarding aerosol vertical distribution over land [24], variation of aerosol height is not considered here to focus on aerosol microphysical parameters. The difference between PODER-3 and 3MI in central wavelengths and spectral response is considered in their simulations. Thus, the observation vector of single-view POLDER-3 measurements contains six-band TOA reflectance and three-band DOLP

$$\begin{aligned}\mathbf{y}_{\mathrm{POLDER-3}} \in [&I_{443}, I_{490}, I_{565}, I_{670}, I_{865}, I_{1020}\\ &\mathrm{DOLP}_{490}, \mathrm{DOLP}_{670}, \mathrm{DOLP}_{865}]^T.\end{aligned} \tag{7}$$

By contrast, the observation vector of single-view 3MI measurements has eight-band TOA reflectance and their DOLP

$$\begin{aligned}\mathbf{y}_{\mathrm{3MI}} \in [&I_{410}, I_{443}, I_{490}, I_{555}, I_{670}, I_{865}, I_{1650}, I_{2130}\\ &\mathrm{DOLP}_{410}, \mathrm{DOLP}_{443}, \mathrm{DOLP}_{490}, \mathrm{DOLP}_{555}\\ &\mathrm{DOLP}_{670}, \mathrm{DOLP}_{865}, \mathrm{DOLP}_{1650}, \mathrm{DOLP}_{2130}]^T.\end{aligned} \tag{8}$$

In the single-view experiment, we fix the solar zenith angle (SZA) at 20° and simulate TOA reflectance and DOLP with view zenith angle (VZA) from 0° to 75° and relative azimuth angle (RAA) from 0° to 180°. For multiview measurements, VZA is set along track from 0° to ±65° with SZA ranging from 0° to 60° [25]. As a result, the MAP measurements of POLDER-3 and 3MI include 126 and 224 observation variables, respectively.

B. State Vector

Consistent with many previous studies [15], [16], aerosols are assumed to be spherical particles with size distribution following a bimodal lognormal function:

$$\frac{\mathrm{d}V}{\mathrm{dln}r} = \sum_{i=1}^{2} \frac{V_0^i}{\sqrt{2\pi}\ln\sigma_g^i} \exp\left[-\frac{\left(\ln r - \ln r_v^i\right)^2}{2\ln^2\sigma_g^i}\right] \tag{9}$$

where V_0 is the total aerosol volume concentration with unit of $\mu\mathrm{m}^3 \cdot \mu\mathrm{m}^{-2}$, and $\mathrm{r_v}$ and σ_g denote the volume geometric median radius and its geometric standard deviation, respectively. The superscript $i = 1$ and 2 here represents a fine and coarse mode, with a size range of 0.01–10 and 0.05–20 μm, respectively. The effective radius r_{eff} can be converted from r_v and σ_g

$$r_{\mathrm{eff}} = r_v \exp\left(-\frac{1}{2}\ln^2\sigma_g\right). \tag{10}$$

Furthermore, the AOD (τ_a) at specific wavelength (λ) can be derived

$$\tau_a(\lambda) = \sum_{i=1}^{2} \frac{3V_0^i Q_{\mathrm{ext}}^i(\lambda)}{4r_{\mathrm{eff}}^i} \tag{11}$$

where Q_{ext} denotes the aerosol extinction efficiency factor, which is the ratio of extinction cross section and the geometric cross section. Aerosol loading is set at 0.5 and 1.0 to represent moderate and heavy pollution, respectively. The fine mode volume fraction (FMF) is set up at 0.8 and 0.2 to represent cases dominated by fine particles and coarse particles, respectively. Considering that different types of size distribution functions have the same r_{eff} and effective variance v_{eff}, r_{eff} and v_{eff} of the fine and coarse modes are retrieved rather than specific size bins with more unknowns [26].

The complex refractive index of aerosol particles is a spectral-dependent optical parameter consisting of real part (MR) and MI, corresponding to the scattering and absorbing

TABLE I
AEROSOL MICROPHYSICAL PARAMETERS

Aerosol Mode	Fine	Coarse
Vol_f [a]	0.109(0.217)	0.027(0.054)
Vol_c [a]	0.133(0.267)	0.533(1.067)
r_{eff}	0.108	2.366
v_{eff}	0.916	0.862
ar [b]	1.379	1.484
br [b]	-0.026	-0.054
ai [b]	0.004	0.007
bi [b]	0.605	-0.081

[a] The subscripts f and c indicate the fine and coarse modes respectively. The volume concentration corresponding to AOD of 0.5 at 550 nm is shown outside the brackets and the result for AOD of 1.0 at 550 nm is shown inside the brackets.
[b] The complex refractive index listed here refer to the fit coefficients obtained by power function ($MR(\lambda) = a_r \times \lambda^{b_r}$, $MI(\lambda) = a_i \times \lambda^{b_i}$) based on the values from the OPAC database. See the text for detailed explanations of a and b.

ability of ambient aerosols. We take a spectral complex refractive index of water-soluble aerosols with a relative humidity of 80% and transported dust from the OPAC (optical properties of aerosols and clouds) database to represent the scattering properties of typical fine and coarse particles [27]. Furthermore, to make full use of the multiwavelength measurement information in retrieving spectral-dependent parameters, we adopt a prior constraint that the complex refractive index is the function of wavelength with fitting coefficients, including a_r, b_r, a_i, and b_i [28]

$$\text{MR}(\lambda) = a_r \times \lambda^{b_r} \tag{12}$$
$$\text{MI}(\lambda) = a_i \times \lambda^{b_i}. \tag{13}$$

Specifically, the OPAC database gives the complex refractive index of each band. We calculate the best fitting of a and b according to (12) and (13) to replace the wavelength-dependent complex refractive index. Thus, unknowns MR and MI that have a number twice of the used satellite bands are streamlined to four coefficients of wavelength. Table I summarizes the aerosol microphysical parameters of the two aerosol modes for input of RT simulations. For the vertical distribution of aerosols, a 2 km vertical profile is utilized with aerosol extinction decreasing exponentially with the height.

To characterize the anisotropy of directional surface reflectance, we select a semiempirical bidirectional reflectance distribution function (BRDF) with the Ross-Thick/Li-Sparse kernels that have been widely used in MODIS land products [29], [30]

$$R(\lambda, \vartheta_v, \vartheta_0, \varphi) = f_{\text{iso}}(\lambda) + f_{\text{vol}}(\lambda) K_{\text{vol}}(\vartheta_v, \vartheta_0, \varphi) + f_{\text{geo}}(\lambda) K_{\text{geo}}(\vartheta_v, \vartheta_0, \varphi) \tag{14}$$

where $f_{\text{iso}}(\lambda)$, $f_{\text{vol}}(\lambda)$, and $f_{\text{geo}}(\lambda)$ denote the spectral weighting parameters for the isotropic scattering, Ross-Thick volume scattering kernel (K_{vol}), and Li-Sparse geometric scattering kernel (K_{geo}) of certain surface types, respectively. Besides wavelength λ, ϑ_v, ϑ_0, and φ represent VZA, SZA, and RAA, respectively. The surface type is assumed to be bare land, which has a moderate brightness in the visible bands. Table II gives the detailed spectral BRDF parameters derived from MODIS products or their approximation. Since the polarized reflectance of land surface is much smaller than the intensity [31], we take the bidirectional polarization distribution function (BPDF) parameter of bare land as known.

TABLE II
BRDF WEIGHTING PARAMETERS OF EACH BAND

Band(nm)	$f_{iso}(\lambda)$	$f_{vol}(\lambda)$	$f_{geo}(\lambda)$
410	0.0457	0.0394	0.0010
443	0.0457	0.0394	0.0010
490	0.0457	0.0394	0.0010
555/565	0.0871	0.0561	0.0083
670	0.0747	0.0614	0.0020
865	0.3841	0.1381	0.0711
1020	0.3520	0.1659	0.0637
1650	0.2550	0.0804	0.0570
2130	0.1475	0.0647	0.0269

In summary, the state vector of 3MI inversion consists of 38 aerosol and surface parameters (32 for POLDER-3): aerosol column volume concentration Vol ($\mu\text{m}^3 \cdot \mu\text{m}^{-2}$), effective radius r_{eff} and its variance v_{eff}, and fitting coefficients (a_r, b_r, a_i, and b_i) of the complex refractive index for the two aerosol modes as well as spectral BRDF parameters

$$\mathbf{x}_{\text{3MI}} \in \Big[\text{Vol}_f, \text{Vol}_c, r_{\text{eff}}^f, v_{\text{eff}}^f, r_{\text{eff}}^c, v_{\text{eff}}^c, a_r^f, b_r^f \\ a_i^f, a_i^f, a_r^c, b_r^c, a_i^c, a_i^c, f_{\text{iso}}(410\text{ nm}) \\ f_{\text{vol}}(410\text{ nm}), f_{\text{geo}}(410\text{ nm}), \ldots\ldots \\ f_{\text{iso}}(2130\text{ nm}) f_{\text{vol}}(2130\text{ nm}), f_{\text{geo}}(2130\text{ nm})\Big]^T \tag{15}$$

$$\mathbf{x}_{\text{POLDER}-3} \in \Big[\text{Vol}_f, \text{Vol}_c, r_{\text{eff}}^f, v_{\text{eff}}^f, r_{\text{eff}}^c, v_{\text{eff}}^c, a_r^f \\ b_r^f, a_i^f, a_i^f, a_r^c, b_r^c, a_i^c, a_i^c, f_{\text{iso}}(443\text{ nm}) \\ f_{\text{vol}}(443\text{ nm}), f_{\text{geo}}(443\text{ m}), \ldots\ldots \\ f_{\text{iso}}(1020\text{ nm}) f_{\text{vol}}(1020\text{ nm}), f_{\text{geo}}(1020\text{ nm})\Big]^T. \tag{16}$$

C. Observation Errors and A Priori

As given by formulas (4) and (5), the DFS and retrieval performance depend on the error quantification for the state of the observation and a prior. Thus, it is crucial to make a realistic description of uncertainty. For the observation errors, we conservatively select a 3% radiometric uncertainty and an absolute DOLP uncertainty of 0.01 based on existing studies for POLDER-3 instrument [23]. With a better calibration accuracy, the radiometric and DOLP uncertainty of 3MI is set to 2% and 0.005, respectively [11].

Table III shows the a priori errors for all retrieved parameters. For the uncertainties of prior knowledge of state parameters, we assume a 100% relative uncertainty for aerosol column volume concentration and 80% for both r_{eff} and v_{eff} [32]. The prior variations of complex refractive index are

TABLE III
A Priori Errors for All Retrieved Parameters *

State vector	A priori error
Vol_f Vol_c	100%
$r_{eff,f}$ $r_{eff,c}$	80%
$v_{eff,f}$ $v_{eff,c}$	80%
ar_f ar_c	0.0443, 0.0027
br_f br_c	0.0228, 0.5191
ai_f ai_c	0.0467, 0.0006
bi_f bi_c	0.0306, 0.7886
$f_{iso}(\lambda)$ $f_{vol}(\lambda)$ $f_{geo}(\lambda)$	20%

* Relative error expressed as a percentage and absolute error expressed as a numerical value.

TABLE IV
Settings of Geometrical Observation in Forward Simulations

Input Parameters	Single-angle observation	Multi-angle observation
Solar zenith angle (SZA)	20°	0°~65°
View zenith angle (VZA)	0°~75°	0°~65°
Relative azimuthal angle (RAA)	0°~180°	0°, 180°
Scattering angle (SCA*)	85°~180°	/

* The scattering angle is not directly used as input to UNL-VRTM, but can be calculated from the geometry of the solar and the observations.
cos(SCA)=cos(VZA)×cos(SZA)+sin(VZA)×sin(SZA)×cos(RAA)

calculated based on daily average inversions (level 1.5) in the Beijing site of Aerosol Robotic Network (AERONET) during 2010–2020, which are 753 records in total. To discriminate between fine and coarse modes, AERONET fine mode fraction of AOD (>0.8 and <0.2) is used. The fitting coefficients and their standard deviation are calculated according to (12) and (13) as a priori error. The weighting coefficients of surface BRDF kernels are assumed to have a relative uncertainty of 20% [14], [15].

D. Forward Model

The unified linearized vector radiative transfer model (UNL-VRTM) is a specific numerical testbed for information content analysis and optimal inversion in atmospheric remote sensing [18]. The main modules of UNL-VRTM include Rayleigh scattering and gas absorption (HITRAN database), aerosol single scattering (linearized Mie scattering and T-matrix code), and a surface BRDF. Also, a linearized vector radiative transfer model (VLIDORT) is integrated to consider multiple scattering of the diffuse radiation of the stratified atmosphere. VLIDORT can calculate the Stokes four-vector parameters (I, Q, U, and V) and their partial derivatives (or Jacobian Matrix $\mathbf{K}$) to each atmospheric and surface parameter. Table IV shows the common scope of satellite observation geometry. To specify atmospheric type for air density profile, the mid-latitude summer type is selected.

IV. Results and Analysis

The aerosol particles can be broadly divided into two categories: fine particles emitted by anthropogenic activities such as fossil fuel combustion and biomass burning fires, and coarse particles mainly from natural sources (e.g., dust and sea salt). Thus, our study intends to analyze the retrieval ability of satellite MAP measurements for aerosols dominated by fine and coarse modes. Fig. 1 shows the simulated spectral and angular variations of satellite TOA reflectance and DOLP for fine-/coarse-dominated aerosols at moderate air pollution (AOD = 0.5) with zero surface reflectance. Strong Rayleigh scattering is concentrated at large VZAs (>60°–70°) at blue bands, especially at 410 nm in near backward directions. While satellite TOA reflectance is at similar levels in visible spectrum for aerosols dominated by both fine and coarse modes, the backward scattering intensity of coarse particles is much higher at near-infrared and shortwave infrared bands.

By contrast, the DOLP of fine particles has high values (>0.3) except in backward directions. Different from scattering intensity, fine particles have marked polarized signals even at shortwave infrared bands with DOLP > 0.2. Despite much lower values than that of fine particles, coarse aerosols have considerable DOLP ranging between 0.2 and 0.5 in visible bands. Fig. 2 gives the phase function (F11) and polarized phase function (−F12/F11) of fine and coarse particles, which can generally explain angular variations of satellite backward measurements with a scattering angle scope of 85°–180°. However, inferring aerosol optical properties by satellite MAP measurements can get complicated with coupled atmosphere-surface signals (see Figure 1S). Quantitative estimation of aerosol information content and sensitivity analysis of POLDER-3 and 3MI measurements to aerosol optical parameters are conducted based on the Bayesian theory.

A. Angular DFS of POLDER-3 and 3MI Aerosol and Surface Parameters

Fig. 3 shows the angular distribution of the DFS for aerosol and surface from POLDER-3 and 3MI measurements. In moderate pollution (AOD = 0.5), aerosol DFS of POLDER-3 ranges from 2.5 to 3.5 for a fine-dominated case and increases to approximately 0.5 for a coarse-dominated case. With enhanced MAP observation, 3MI has a fine-dominated aerosol DFS of 4.0–6.0 with an increase of ~1.0 for coarse-dominated. Although the phase function of fine particles is obviously higher in the backward direction, their scattering cross section decreases largely with wavelengths. By contrast, the more scattering information of coarse particles in near-infrared and shortwave infrared bands leads to higher DFS for coarse-dominated conditions.

Compared with POLDER-3, the extended spectrum of 3MI substantially enhances MAP detection ability for coarse-dominated aerosols. With larger aerosol loading (AOD = 1.0), the DFS values increase by ~1.0–2.0 due to more contribution from aerosols. Correspondingly, the DFS of 3MI surface parameters ranges from 5.5 to 7.0 with AOD = 0.5 and decreases by ~2.0 at AOD = 1.0. Also, the enhanced 3MI

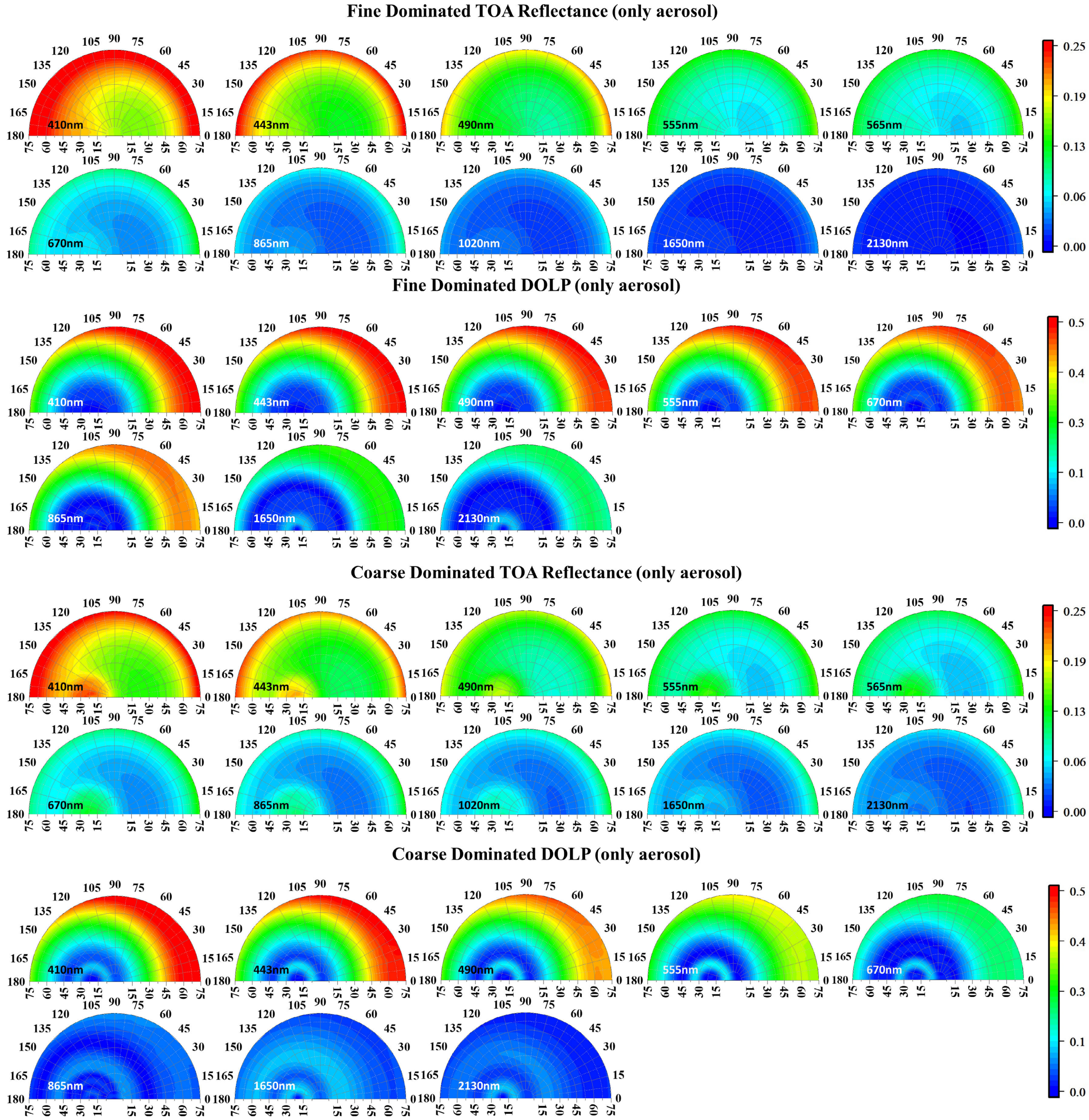

Fig. 1. TOA reflectance and DOLP in the fine dominant case and coarse dominant case when AOD = 0.5 and SZA of 20°, respectively (consider aerosols only). The polar radius represents VZA from 0° to 75° and the polar angle is RAA from 0° to 180°. (Scattering angle ranging from 85° to 180°.)

observations have a notable improvement in characterizing surface BRDF.

To further examine the effective sensitivity of each 3MI measurement to infer retrieved aerosol parameters, we compute the EN-Jacobian matrix at AOD = 0.5 (Figs. 4 and 5). As shown in Figs. 4(a1) and 5(a1), satellite spectral radiances are very sensitive to Vol_f at visible bands, even for coarse-dominated conditions. However, there is little information of fine particles in longer wavelengths except at large VZAs (>60°) and small scattering angles (<100°). By contrast, satellite radiances at 865 and 2130 nm have a stable and large sensitivity to Vol_c. While both I and DOLP have increasing information of Vol_f at a coarse-dominated case as the scattering angle decreases from 140° to 80°, they are generally not sensitive to Vol_c at the fine-dominated condition. Thus, accurate satellite retrieval of Vol_c or AOD of coarse mode can be a challenge in thefine-dominated condition even for 3MI measurements.

While the sensitivity of I to r_{eff}^f gets much lower at fine-dominated conditions compared with Vol_f, DOLP is very sensitive to r_{eff}^f and v_{eff}^f fortunately. While both I and DOLP have abundant information of r_{eff}^c and v_{eff}^c, only DOLP is sensitive to r_{eff} and v_{eff} of nondominant particles with VZAs >40°. For the complex refractive index, both I and DOLP have stable EN Jacobians (∼2–4) to a_r^f and b_r^f in a fine-dominated case but exhibits little information for b_r^c in coarse-dominated aerosols. The sensitivity of I and DOLP to the MI is lower than that of the MR, especially for the coefficient a_i. Consistent with ground observations [15], [33], the information of complex refractive index is limited in satellite measurements, and certain coefficients, such as b_r^c and a_i, highly depend on VZAs (>55°). In Fig. 4(i2), the infrared band, which includes the 1650- and 2130-nm bands where coarse-mode particles are located, increases as they approach the backscattering direction: the DOLP increases with increasing a_r^c. According to our power function fit relationship, an increase in

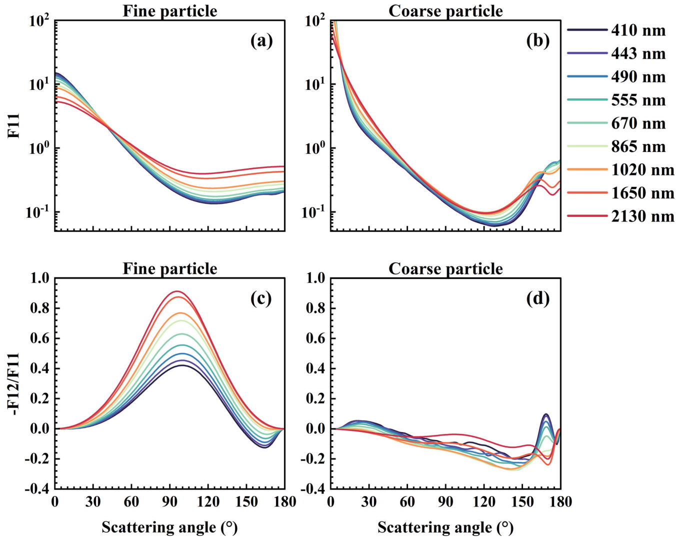

Fig. 2. Phase function of radiance component (F11) and polarization component (–F12/F11) as a function of scattering angle. (a) F11 phase function for fine particulate; (b) F11 phase function for coarse particulate; (c) –F12/F11 phase function for fine particulate; and (d) –F12/F11 phase function for coarse particulate.

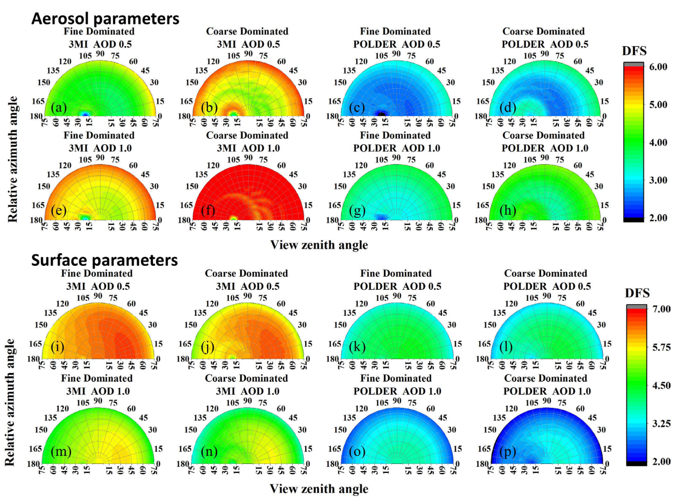

Fig. 3. DFS of aerosol (a–h) and surface parameters (i–p) polar coordinates plotted for POLDER and 3MI in single-view observation mode for a given aerosol-dominated modes and AOD. The polar coordinates are defined similarly to Fig. 1.

a_r^c represents an enhancement of aerosol particle scattering. The EN-Jacobian of a_r^c at scattering angles less than 140° mutates to less than 0. This result captures to some extent the change in the polarization phase function of coarse particles in the backscattering direction [e.g., Fig. 2(d)], although the scattering angles do not strictly match.

It should be stated that the fine and coarse mode aerosol is selected as weak-absorbing and absorbing, respectively, which can reduce the sensitivity to MI of fine particles and MR of the coarse aerosols. On the other hand, the information of nondominated aerosols can increase as AOD. Generally, the expanded measurement spectrum and the corresponding polarization can increase aerosol information, though not for all the parameters and all the view geometries. Thus, it is necessary to integrate the multiangle measurement information into the retrieval.

B. Total DFS of Aerosol and Surface in Satellite MAP Measurement

Fig. 6 shows how the total DFS of aerosol in 3MI and POLDER-3 measurements changes with SZAs. By integrating their multiangle observations, the total DFS of 14 retrieved aerosol parameters increases from no more than 6 to ∼10–12 for 3MI measurements with AOD = 0.5 or 1.0. By contrast, the DFS of the 14 retrieval parameters is improved from ∼3.5 to ∼6–8 for POLDER-3 measurements. Unlike POLDER-3, the total DFS from 3MI in the fine-dominated condition is about ∼3 higher than that in a coarse-dominated case. Although the expanded spectrum of 3MI can provide additional information regarding coarse aerosols, these coarse particles can also reduce the information of surface BRDF parameters in near-infrared and shortwave bands. Because of the counteracting effect of aerosol and surface in information content, there is only a ∼1 difference in DFS for AOD of 0.5 and 1.0. Contrary to the information content of single-angle measurements (see Fig. 3), the total DFS from 3MI and POLDER-3 is higher by ∼1.5 with an AOD of 0.5 rather than 1.0.

Meanwhile, large SZAs allow a wider range of scattering angles and a longer optical path, which in turn contains more information of aerosols. Compared with POLDER-3, the enhanced 3MI observation has a higher total DFS by ∼2–4. To further explore the DFS components from MAP measurements, the DFS of retrieved aerosol and surface parameters is analyzed in Figs. 7–12. It can be seen that multiangle measurements have greatly improved the DFS (∼0.85–1.0) of both Vol_f and Vol_c (see Fig. 7), especially for Vol_c in a fine-dominated case. The DFS of Vol_f and Vol_c is at similar levels for POLDER-3 and 3MI, except for an obvious difference in Vol_c of fine-dominated case.

Similar to volume concentration, MAP measurements, such as 3MI and POLDER-3, have a high DFS (∼0.85–1.0) for effective radius of both fine and coarse particles (see Fig. 8), even with a low fraction of AOD (e.g., 0.2). Also, 3MI has a larger DFS than POLDER-3 for the nondominated aerosol mode. There is a notable decrease in the DFS of effective variance for 3MI as well as a much larger magnitude (∼0.4–0.5) for POLDER-3. In contrast, the DFS of complex refractive index highly depends on the ability of MAP measurements and AOD. The MR is more sensitive to satellite detection ability with 3MI having ∼0.2–0.3 higher DFS than POLDER-3. The largest uncertainties are concentrated in the MI in fine-dominated conditions. Even with the 3MI measurements at a high AOD of 1.0, the DFS of a_i^f and b_i^f is only ∼0.5–0.6 and ∼0.2–0.3 (see Fig. 9), respectively. As mentioned above, the strong scattering of fine mode aerosols we used can be the main cause. Correspondingly, the DFS of a_i^c and b_i^c for the absorbing coarse particles in the coarse-dominated case is much higher (see Fig. 10).

Figs. 11 and 12 show the DFS of surface BRDF parameters at 443 and 865 nm, respectively. Considering the large

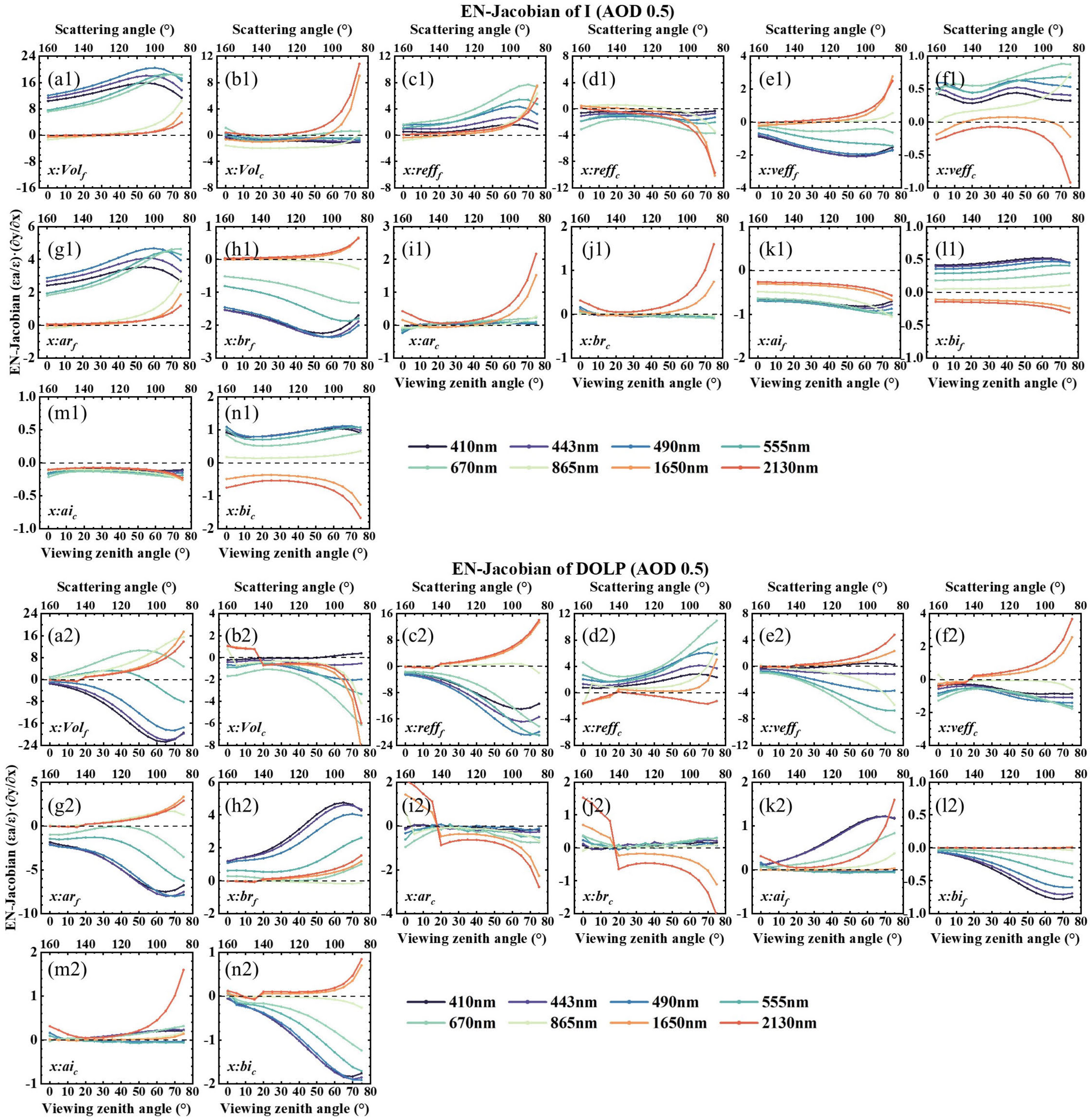

Fig. 4. EN Jacobians of stokes I component and DOLP with respect to retrieved parameters: Vol_f (a1 and a2), Vol_c (b1 and b2), reff_f (c1 and c2), reff_c (d1 and d2), veff_f (e1 and e2), veff_c (f1 and f2), ar_f (g1 and g2), br_f (h1 and h2), ar_c (i1 and i2), br_c (j1 and j2), ai_f (k1 and k2), bi_f (l1 and l2), ai_c (m1 and m2), bi_c (n1 and n2). Simulations use fine dominated mode with AOD of 0.5.

contribution of atmosphere in blue bands, surface reflectance is dominated by isotropic scattering with very weak BRDF effects. f_{iso} from 3MI measurements has a DFS of around 0.9 for moderate pollution and gets higher at 865 nm. With no polarization measurement and lower calibration accuracy, f_{iso} of POLDER-3 has a lower DFS by ~0.4. As the wavelength gets longer at 865 nm, the volume and geometric scattering of soil surface becomes stronger with less influence by aerosols. In particular, the DFS of the volume scattering increases largely with the SZAs with the lowest magnitude.

C. A Posteriori Error of Satellite MAP Retrievals and Potential Uncertainties

A posteriori error $\hat{S}$ quantifies the statistical uncertainties of each retrieved parameter due to measurement noise and prior errors. As shown in the right of Figs. 7–12, the retrieval

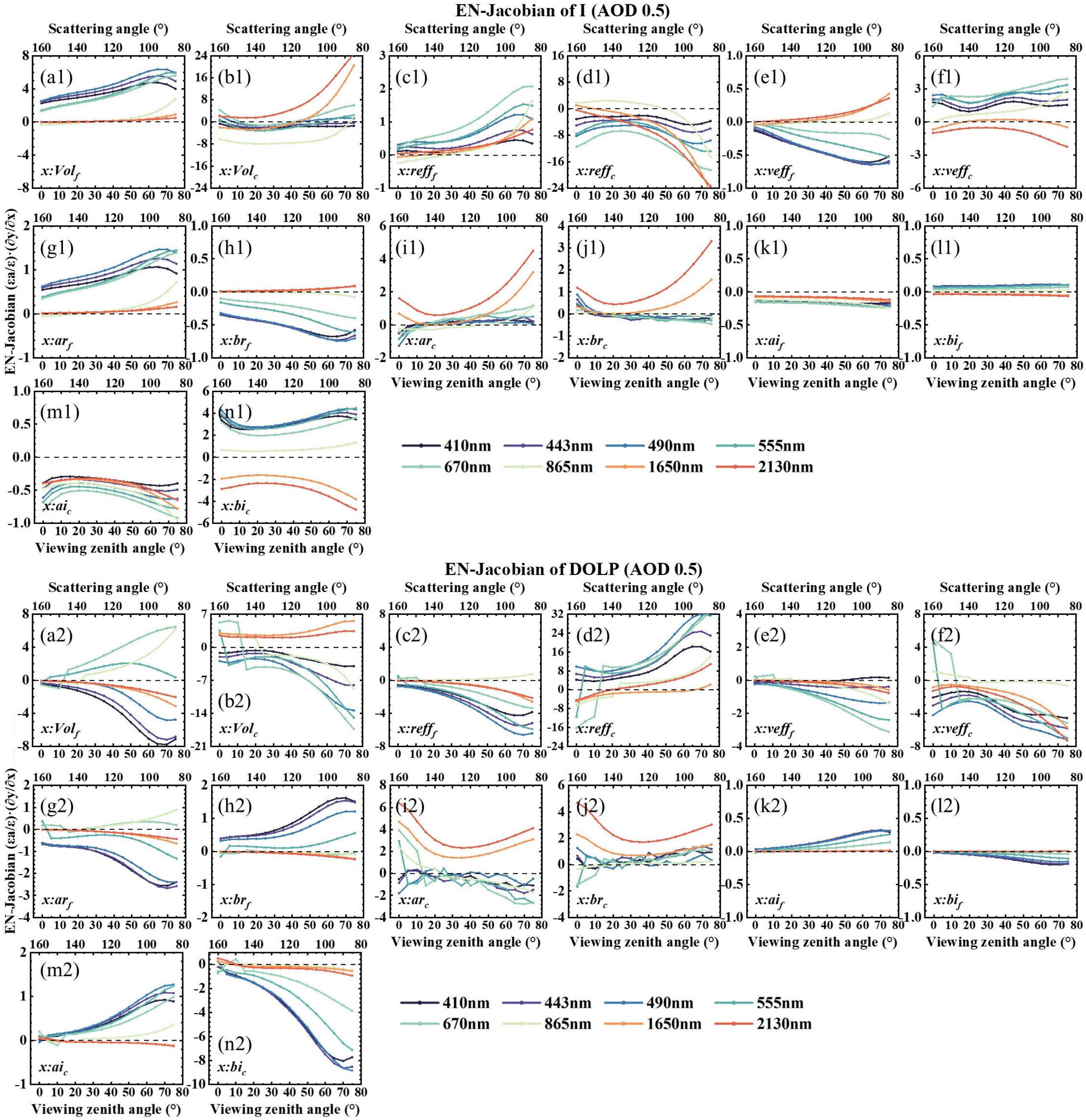

Fig. 5. EN Jacobians of stokes I component and DOLP with respect to retrieved parameters: Vol_f (a1 and a2), Vol_c (b1 and b2), reff_f (c1 and c2), reff_c (d1 and d2), veff_f (e1 and e2), veff_c (f1 and f2), ar_f (g1 and g2), br_f (h1 and h2), ar_c (i1 and i2), br_c (j1 and j2), ai_f (k1 and k2), bi_f (l1 and l2), ai_c (m1 and m2), bi_c (n1 and n2). Simulations use coarse-dominated mode with AOD of 0.5.

errors of 3MI are much lower than those of POLDER-3 by ~50% due to more measurement information and higher calibration accuracy. Despite a very low retrieval error within 2%–3% for Vol_f in fine-dominated conditions, Vol_c has larger uncertainties around ~3%–10%, especially for high AODs in a coarse-dominated case. As a key parameter determining fraction of aerosol and surface contribution to satellite TOA reflectance, the higher retrieval errors of Vol_c can be caused by more influence on spectral surface reflectance from coarse particles. Meanwhile, the retrieval of effective radius exhibits similar performance with a positive dependence on AOD for dominant aerosol sizes [see Fig. 8(e) and (g)]. The retrieval uncertainties of r_{eff}^{c} reach as high as 30% and 50% in fine-dominant conditions for 3MI and POLDER-3, respectively. By contrast, the retrieval error of $\upsilon_{\mathrm{eff}}^{c}$ (~15%) is much smaller than that of $\upsilon_{\mathrm{eff}}^{f}$ (~30%) partly due to its large variations.

While the retrieval accuracy of MR is upgraded by ~50% compared with that of POLDER-3, the improvement of MI

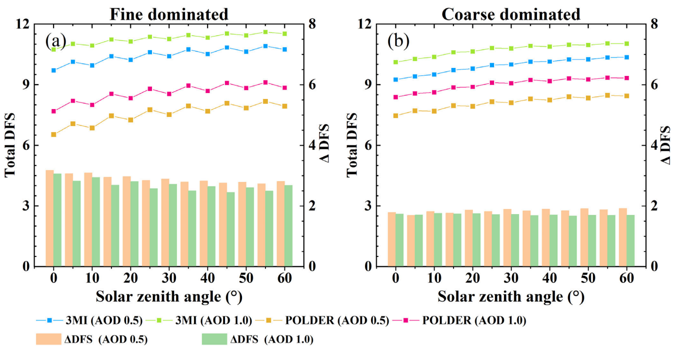

Fig. 6. DFS as a function of SZA for retrieving aerosol parameters (including volume concentrations, particle size parameters, and complex refractive index fitting coefficients for both modes, 14 in total) when using aerosol type of (a) fine dominated and (b) coarse dominated. Four differently colored curves denote the scenarios for POLDER and 3MI at an AOD of 0.5 and 1.0, respectively. The histograms give the increase in DFS for 3MI compared to POLDER for AOD of 0.5 and 1.0.

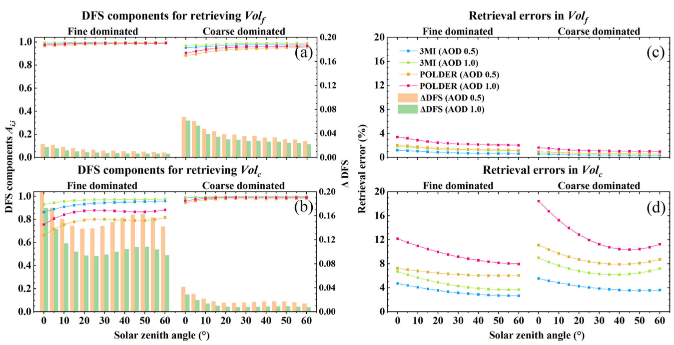

Fig. 7. DFS components and posteriori errors for retrieving (a) and (c) Vol_f and (b) and (d) Vol_c, respectively, as a function SZAs. In each panel, the left is for the fine mode and the right is for the coarse mode. The meaning of the legend is the same as in Fig. 6.

retrieval is remarkable mainly in high AODs (>1.0) with 3MI measurements (see Figs. 9 and 10). The retrieval error of MI from 3MI at AOD = 0.5 is slightly smaller than that from POLDER-3 at AOD = 1.0. By calculating the mean values of their absolute errors (see Figure 2S), it is found that satellite MAP retrieval of complex refractive index has a close accuracy with the results from ground-based Sun photometer. Retrieval errors of coefficient a_r lead to an uncertainty of MR^f and MR^c by ∼0.02 and ∼0.01, respectively. The retrieval errors of MR^f and MR^c by b_r are around −0.01 and decrease largely with the wavelength, which may partly compensate the uncertainties from ar. There is a high retrieval accuracy (<0.0005) for MI^c with the absorbing assumption. By contrast, retrieval errors of a_i and b_i lead to uncertainties of MI^f by ∼0.001–0.002 and −0.0005 to (−0.001), respectively.

The posterior errors of surface BRDF are very small with most parameters within 1%–2% (see Figs. 11 and 12). For the longer bands such as 865 nm, the weighting coefficient of volumetric scattering kernel has a slightly higher uncertainty below 3%. It should be stated that a soil surface type with 20% prior error and moderate pollution is assumed. The retrieval errors of BRDF factors can be larger for heavy pollution and other surface types such as vegetation and urban regions.

Our assumptions regarding aerosol and surface cannot fully cover all the common conditions. Generally, the estimation

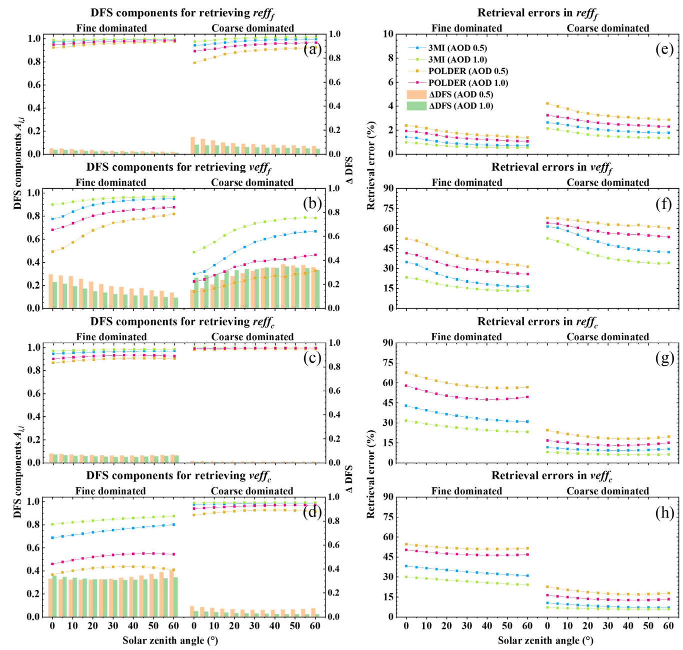

Fig. 8. DFS components and posteriori errors for retrieving (a) and (e) reff_f, (b) and (f) veff_f, (c) and (g) reff_c, and (d) and (h) veff_c as a function SZAs. In each panel, the left is for the fine mode and the right is for the coarse mode. The meaning of the legend is the same as in Fig. 6.

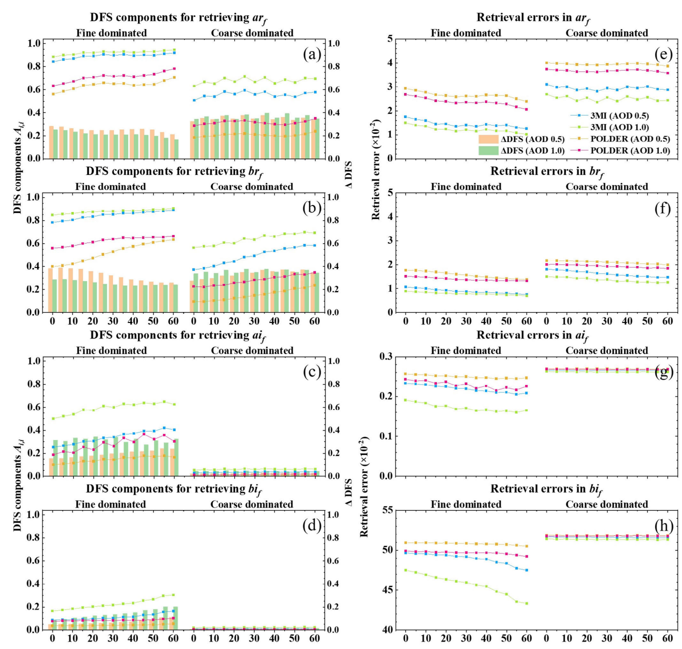

Fig. 9. DFS components and posteriori errors for retrieving the fit coefficients for fine modal aerosol complex refractive index with power-law dependence. (a) and (e) ar_f, (b) and (f) br_f, (c) and (g) ai_f, and (d) and (h) bi_f. In each panel, the left is for the fine mode and the right is for the coarse mode. The meaning of the legend is the same as in Fig. 6.

of the retrieval ability of satellite MAP measurements in a typical case can give a fundamental reference for development of inversion algorithm and corresponding uncertainties. While the enhanced 3MI observations greatly increase the information content of aerosols and surface, some aerosol parameters, such as MI of the complex index, remain subject to considerable retrieval errors. Due to double unknowns

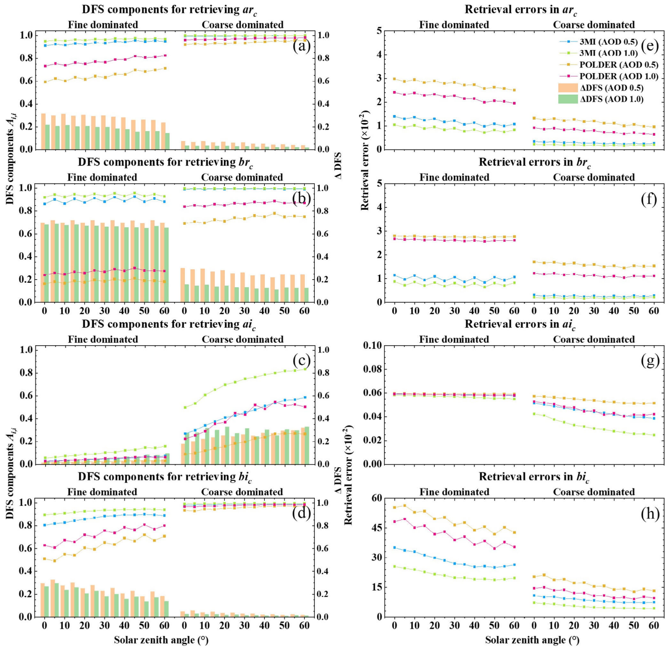

Fig. 10. DFS components and posteriori errors for retrieving the fit coefficients for coarse modal aerosol complex refractive index with power-law dependence. (a) and (e) Ar$_f$, (b) and (f) br$_f$, (c) and (g) ai$_f$, and (d) and (h) bi$_f$. In each panel, the left is for the fine mode and the right is for the coarse mode.

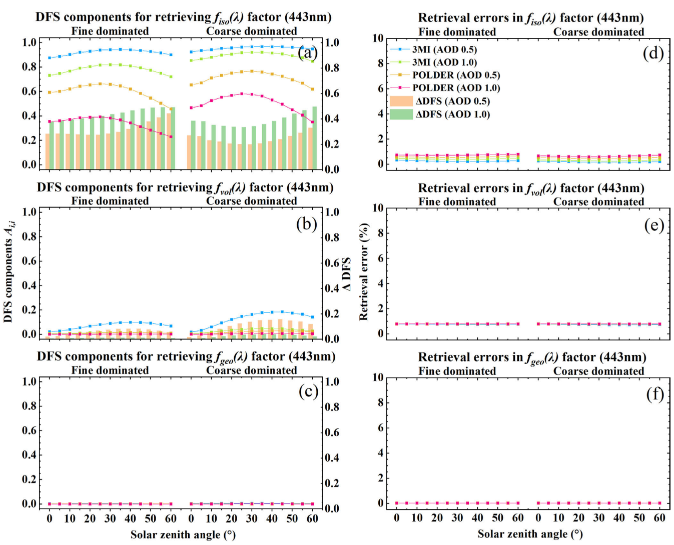

Fig. 11. DFS components and posteriori errors for retrieving surface parameters in 443 nm, including (a) and (d) isotropic factor, (b) and (e) volumetric factor, and (c) and (f) geometric-optical factor, respectively.

of the number of spectral bands, a prior assumption of empirical function between wavelength and MR or MI is utilized. In the actual inversion, prior information, such as known aerosol types with fixed MR and MI, can be selected. In addition, both fine and coarse particles are considered spherical in our analysis. As shown by Dubovik et al. [34] and Deuzé et al. [35], the sensitivity of linear polarization is weak for the MR of refractive index of large nonspherical particles. Thus, the information content and retrieval accuracy in our analysis may be degraded for nonspherical coarse particles, which will be further improved in our future efforts.

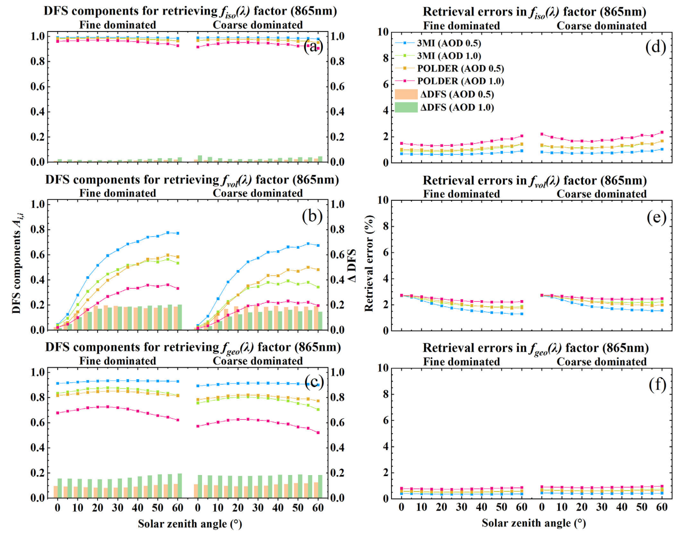

Fig. 12. DFS components and posteriori errors for retrieving surface parameters in 865 nm, including (a) and (d) isotropic factor, (b) and (e) volumetric factor, and (c) and (f) geometric-optical factor, respectively.

D. Discussion

The recent POLDER-3 retrievals, such as General Retrieval of Atmosphere and Surface Properties (GRASP) algorithm, have exhibited the great potential of MAP measurements in characterizing aerosol optical/microphysical properties [36]. However, GRASP retrievals, such as POLDER coarse AOD and single scattering albedo, have considerable uncertainties. POLDER AOD from GRASP optimized inversion has an obviously lower accuracy than that from GRASP components retrieval with fixed aerosol types, which can be caused by the influence of aerosol parameters with low DFS. On the other hand, assumptions, such as the same component for both fine and coarse particles, are utilized in GRASP POLDER-3 retrievals due to limited information content, which can be quite different from the actual situation. Thus, it is necessary to consider aerosol information content or DFS in developing an MAP retrieval algorithm, especially for the emerging MAP satellite instruments with different spectral channels and corresponding polarimetric measurements. Another key problem in MAP retrieval is to constrain aerosol parameters with low DFS by effective prior knowledge or assumptions. Considering the complicated chemical/physical properties of aerosols in regional and global scales, there is still an urgent need of clear and sufficient references to better constrain satellite MAP retrievals.

V. Conclusion

With the urgent need in quantifying aerosol climate effects and aerosol scattering contribution in the retrieval of greenhouse gases, a series of dedicated satellite missions with enhanced MAP instruments will be launched in the near future. However, different spectrum ranges, spectral bands, and viewing angles of these satellite instruments exert a marked challenge in the availability and consistency of their retrieved aerosol optical/microphysical parameters. To fully explore the retrieval ability of common satellite MAP instruments, we estimate information content and posterior errors of each aerosol optical/microphysical parameters from POLDER-3 and 3MI measurements based on the Bayesian optimization theory.

Our results show that POLDER-3 observations have high DFS in retrieving volume concentration and effective radius, with larger retrieval errors (∼10% and ∼15%) for coarse aerosols. In particular, retrieval uncertainties in effective radius of coarse particles exceed 50%–60% in a fine-dominated case. Furthermore, the large decline of DFS values in effective variance of effective radius and aerosol absorption from POLDER-3 measurements leads to considerable posteriori errors (>30%–50%), indicating insufficient information content in inferring all the unknowns.

Compared with POLDER-3, enhanced MAP measurements of 3MI have higher DFS of aerosols by ∼1.8–3.5 and decrease the retrieval errors by nearly 50% for most microphysical parameters. The extended spectrum and polarimetric measurements in most channels from 3MI provide more information regarding aerosol optical/microphysical properties. The additional shortwave infrared bands in 3MI have greatly enhanced the sensitivity of MAP measurements to volume concentration and scattering ability of coarse particles. However, aerosol parameters, such as volume concentration and effective radius of coarse particles, only exhibit notable observational sensitivity in relatively small scattering angles (<120°) or large viewing angles (>50°), demonstrating the necessity to set more directional measurements at large viewing angles. It should be noted that there are still substantial uncertainties (∼30%) in certain 3MI retrievals such as effective radius of coarse particles in fine-dominated conditions, which usually appear in downstream polluted regions of dust sources. Besides upgrading satellite instruments, priori knowledge from existing observations should be used to constrain retrieved aerosol optical/microphysical parameters with low DFS.

Acknowledgment

This study was supported by the National Science Foundation of China (Grant 41830109 and Grant 42271382). Jun Wang's participation is made possible through the in-kind support from the University of Iowa. The authors also thank Dr. Xi Chen for the help in DFS calculation.

References

[1] D. Rosenfeld et al., "Global observations of aerosol-cloud-precipitation-climate interactions," *Rev. Geophys.*, vol. 52, no. 4, pp. 750–808, Dec. 2014.

[2] J. Hansen, M. Sato, and R. Ruedy, "Radiative forcing and climate response," *J. Geophys. Res., Atmos.*, vol. 102, no. D6, pp. 6831–6864, 1997.

[3] K. S. Carslaw et al., "Large contribution of natural aerosols to uncertainty in indirect forcing," *Nature*, vol. 503, no. 7474, p. 67, Nov. 2013.

[4] P. J. Landrigan, "Air pollution and health," *Lancet Public Health*, vol. 2, no. 1, pp. e4–e5, 2017.

[5] M. Tao et al., "Spatial oscillation of the particle pollution in eastern China during winter: Implications for regional air quality and climate," *Atmos. Environ.*, vol. 144, pp. 100–110, Nov. 2016.

[6] M. Tao et al., "Performance of MODIS high-resolution MAIAC aerosol algorithm in China: Characterization and limitation," *Atmos. Environ.*, vol. 213, pp. 159–169, Sep. 2019.

[7] M. Tao et al., "Characterization of aerosol type over East Asia by 4.4 km MISR product: First insight and general performance," *J. Geophys. Res., Atmos.*, vol. 125, no. 13, 2020, Art. no. e2019JD031909.

[8] M. D. King, Y. J. Kaufman, D. Tanré, and T. Nakajima, "Remote sensing of tropospheric aerosols from space: Past, present, and future," *Bull. Amer. Meteorol. Soc.*, vol. 80, pp. 2229–2260, Jul. 1999.

[9] O. Dubovik et al., "Statistically optimized inversion algorithm for enhanced retrieval of aerosol properties from spectral multi-angle polarimetric satellite observations," *Atmos. Meas. Techn.*, vol. 4, no. 5, pp. 975–1018, 2011.

[10] O. Dubovik et al., "Polarimetric remote sensing of atmospheric aerosols: Instruments, methodologies, results, and perspectives," *J. Quant. Spectrosc. Radiat. Transf.*, vol. 224, pp. 474–511, Feb. 2019.

[11] B. Fougnie et al., "The multi-viewing multi-channel multi-polarisation imager—Overview of the 3MI polarimetric mission for aerosol and cloud characterization," *J. Quant. Spectrosc. Radiat. Transf.*, vol. 219, pp. 23–32, Nov. 2018.

[12] X. Zhang et al., "Extensive characterization of aerosol optical properties and chemical component concentrations: Application of the GRASP/Component approach to long-term AERONET measurements," *Sci. Total Environ.*, vol. 812, Mar. 2022, Art. no. 152553.

[13] F.-M. Bréon, A. Vermeulen, and J. Descloitres, "An evaluation of satellite aerosol products against sunphotometer measurements," *Remote Sens. Environ.*, vol. 115, no. 12, pp. 3102–3111, Dec. 2011.

[14] X. Chen et al., "Angular dependence of aerosol information content in CAPI/TanSat observation over land: Effect of polarization and synergy with a-train satellites," *Remote Sens. Environ.*, vol. 196, pp. 163–177, Jul. 2017.

[15] X. Xu and J. Wang, "Retrieval of aerosol microphysical properties from AERONET photopolarimetric measurements: 1. Information content analysis," *J. Geophys. Res., Atmos.*, vol. 120, no. 14, pp. 7059–7078, Jul. 2015.

[16] X. Xu et al., "Retrieval of aerosol microphysical properties from AERONET photopolarimetric measurements: 2. A new research algorithm and case demonstration," *J. Geophys. Res., Atmos.*, vol. 120, no. 14, pp. 7079–7098, 2015.

[17] G. Fu and O. Hasekamp, "Retrieval of aerosol microphysical and optical properties over land using a multimode approach," *Atmos. Meas. Techn.*, vol. 11, no. 12, pp. 6627–6650, Dec. 2018.

[18] J. Wang et al., "A numerical testbed for remote sensing of aerosols, and its demonstration for evaluating retrieval synergy from a geostationary satellite constellation of GEO-CAPE and GOES-R," *J. Quant. Spectrosc. Radiat. Transf.*, vol. 146, pp. 510–528, Oct. 2014.

[19] S. Sanghavi, R. Nelson, C. Frankenberg, and M. Gunson, "Aerosols in OCO-2/GOSAT retrievals of XCO_2: An information content and error analysis," *Remote Sens. Environ.*, vol. 251, Dec. 2020, Art. no. 112053.

[20] M. Choi et al., "Aerosol profiling using radiometric and polarimetric spectral measurements in the O_2 near infrared bands: Estimation of information content and measurement uncertainties," *Remote Sens. Environ.*, vol. 253, Feb. 2021, Art. no. 112179.

[21] X. Chen, X. Xu, J. Wang, and D. J. Diner, "Can multi-angular polarimetric measurements in the oxygen—A and B bands improve the retrieval of aerosol vertical distribution?" *J. Quant. Spectrosc. Radiat. Transf.*, vol. 270, Aug. 2021, Art. no. 107679.

[22] C. D. Rodgers, *Inverse Methods for Atmospheric Sounding: Theory and Practice*. Singapore: World Scientific, 2000.

[23] D. Tanre et al., "Remote sensing of aerosols by using polarized, directional and spectral measurements within the a-Train: The PARASOL mission," *Atmos. Meas. Techn.*, vol. 4, no. 7, pp. 1383–1395, 2011.

[24] X. G. Xu et al., "Passive remote sensing of altitude and optical depth of dust plumes using the oxygen A and B bands: First results from EPIC/DSCOVR at Lagrange-1 point," *Geophys. Res. Lett.*, vol. 44, no. 14, pp. 7544–7554, Jul. 2017.

[25] B. Fougnie et al., "Aerosol retrieval from space–how does geometry of acquisition impact our ability to characterize aerosol properties," *J. Quant. Spectrosc. Radiat. Transf.*, vol. 256, Nov. 2020, Art. no. 107304.

[26] J. E. Hansen and L. D. Travis, "Light scattering in planetary atmospheres," *Space Sci. Rev.*, vol. 29, no. 4, pp. 55–56, 1976.

[27] M. Hess, P. Koepke, and I. Schult, "Optical properties of aerosols and clouds: The software package OPAC," *Bull. Amer. Meteorol. Soc.*, vol. 79, no. 5, pp. 831–844, 1998.

[28] O. Dubovik and M. D. King, "A flexible inversion algorithm for retrieval of aerosol optical properties from Sun and sky radiance measurements," *J. Geophys. Res., Atmos.*, vol. 105, no. D16, pp. 20673–20696, 2000.

[29] W. Lucht, C. B. Schaaf, and A. H. Strahler, "An algorithm for the retrieval of albedo from space using semiempirical BRDF models," *IEEE Trans. Geosci. Remote Sens.*, vol. 38, no. 2, pp. 977–998, Mar. 2000.

[30] C. B. Schaaf et al., "First operational BRDF, albedo nadir reflectance products from MODIS," *Remote Sens. Environ.*, vol. 83, nos. 1–2, pp. 135–148, Nov. 2002, doi: 10.1016/S0034-4257(02)00091-3.

[31] F. Maignan, F.-M. Bréon, E. Fédèle, and M. Bouvier, "Polarized reflectances of natural surfaces: Spaceborne measurements and analytical modeling," *Remote Sens. Environ.*, vol. 113, no. 12, pp. 2642–2650, Dec. 2009.

[32] F. Waquet et al., “Polarimetric remote sensing of aerosols over land,” *J. Geophys. Res., Atmos.*, vol. 114, no. D1, 2009.

[33] O. Dubovik et al., “Variability of absorption and optical properties of key aerosol types observed in worldwide locations,” *J. Atmos. Sci.*, vol. 59, no. 3, pp. 590–608, 2002.

[34] O. Dubovik et al., “Application of spheroid models to account for aerosol particle nonsphericity in remote sensing of desert dust,” *J. Geophys. Res., Atmos.*, vol. 111, no. D11, 2006.

[35] J. L. Deuzé et al., “Remote sensing of aerosols over land surfaces from POLDER-ADEOS-1 polarized measurements,” *J. Geophys. Res., Atmos.*, vol. 106, no. D5, pp. 4913–4926, 2001.

[36] C. Chen et al., “Validation of GRASP algorithm product from POLDER/PARASOL data and assessment of multi-angular polarimetry potential for aerosol monitoring,” *Earth Syst. Sci. Data*, vol. 12, no. 4, pp. 3573–3620, Dec. 2020.

Wenhui Dong received the B.S. degree from the China University of Geosciences, Wuhan, China, in 2019. She is currently pursuing the M.S. degree with the School of Geography and Information Engineering, China University of Geosciences, Wuhan, China, with a focus on forward mechanism and sensitivity of aerosol retrieval in satellite remote sensing technology.

Minghui Tao received the Ph.D. degree from the Chinese Academy of Sciences (CAS), Beijing, China, in 2013.

He worked with the Institute of Remote Sensing and Digital Earth, CAS, from 2013 to 2017. Since 2018, he has been working with the China University of Geosciences (CUG), Wuhan, China. He is currently a Professor with the School of Geography and Information Engineering. He is mainly engaged in satellite remote sensing and atmospheric environment research, including atmospheric environmental remote sensing inversion algorithms, deep learning remote sensing, and geographic information system (GIS) development and application.

Xiaoguang Xu received the Ph.D. degree in earth and atmospheric sciences from the University of Nebraska–Lincoln, Lincoln, NE, USA, in 2015.

He is currently a Research Scientist at the University of Maryland, Baltimore County, Baltimore, MD, USA. He has developed aerosol retrieval algorithms for both satellite and ground-based remote sensing platforms. He is the primary developer of a numerical testbed for remote sensing of aerosol known as UNL-VRTM (https://unl-vrtm.org). His research area has focused on the development of retrieval algorithms, data assimilation of aerosol remote sensing data, with emphasis on the integration of satellite remote sensing and global models to characterize aerosol emitting sources, distributions, as well as their climate and environmental impacts.

Jun Wang received the Ph.D. degree in atmospheric sciences from the University of Alabama–Huntsville, Huntsville, AL, USA, in 2005.

He is currently a Professor with the Department of Chemical and Biochemical Engineering, The University of Iowa, Iowa City, IA, USA, where he also serves as a James E. Ashton Professor in Engineering and the Assistant Director of the Iowa Technology Institute. He is mainly engaged in interaction between atmospheric composition and climate change; and impacts of aerosols on air quality, weather, and climate. His research is related to cloud and trace gases, air quality and public health, irrigation, land use, fire, agriculture, and climate change, as well as renewable (solar and wind) energy.

Dr. Wang is the Chair of the Department of Chemical and Biochemical Engineering, The University of Iowa.

Yi Wang received the Ph.D. degree in geoinformatics from the University of Iowa, Iowa City, IA, USA, in 2021.

He joined the University of Iowa as a Post-Doctoral Research Scholar. He is currently a Professor at the School of Geography and Information Engineering, China University of Geosciences, Wuhan, China. He is mainly engaged in research related to remote sensing and modeling of atmospheric environment, including satellite remote sensing of aerosols, assimilation of atmospheric environment satellite data, inversion of pollution source emission inventory, and deep learning of atmospheric environment models.

Lunche Wang received the Ph.D. degree from the State Key Laboratory of Information Engineering in Surveying, Mapping and Remote Sensing, Wuhan University, Wuhan, China, in 2015.

He is a Professor with the School of Geography and Information Engineering, China University of Geosciences, Wuhan. His research interests include climate change and extreme climate, aerosol and air quality, atmospheric radiation and surface energy balance, and surface vegetation and environmental change.

Yinyu Song received the B.E. degree from Northeastern University, Shenyang, China, in 2018. She is currently pursuing the M.E. degree from the School of Geography and Information Engineering, China University of Geosciences, Wuhan, China, with a focus on research of retrieving aerosol parameters based on deep learning.

Meng Fan received the B.S. degree in remote sensing science and technology from the Shandong University of Science and Technology, Qingdao, China, in 2009, and the Ph.D. degree in cartography and geographic information system from the Institute of Remote Sensing and Digital Earth, Chinese Academy of Sciences, Beijing, China, in 2014.

She is currently an Associate Researcher of Aerospace Information Research Institute, Chinese Academy of Sciences. Her research interests include remote sensing of atmospheric chemical components, aerosol scattering simulation, and satellite-based thermal anomaly detection.

Liangfu Chen received the Ph.D. degree in geography from the Institute of Remote Sensing and Geographical Information System, Peking University, Beijing, China, in 1999.

He is currently a Professor with the Aerospace Information Research Institute, Chinese Academy of Sciences, Beijing. Since 2004, he has led an 863 project of China “multi-source satellite remote sensing technology of atmospheric pollution monitoring” and the Knowledge Innovation Program of Chinese Academy of Sciences. His research interests include the retrieval and application of atmosphere aerosol and trace gases based on remote sensing data.